crystals

MDPI

Article

Numerical Simulation Analysis of Laser Ultrasonic Detection of Defects in Silicon Carbide

Yuan Yin, Jinbao Xia *, Hongkun Nie, Bo Yao, Daofa Sun, Longnan Ma, Ruihang Li, Zihao Li and Baitao Zhang

State Key Laboratory of Crystal Materials, Institute of Novel Semiconductors, Shandong University, Jinan 250100, China; yy1812286895@163.com (Y.Y.); niehongkun2011@163.com (H.N.); yaobo@sdu.edu.cn (B.Y.); sundaofa0301@163.com (D.S.); 202314066@mail.sdu.edu.cn (L.M.); l782964559@163.com (R.L.); 15315131408@163.com (Z.L.); btzhang@sdu.edu.cn (B.Z.)

* Correspondence: jinbaoxia413@sdu.edu.cn

Abstract: Silicon carbide (SiC) is widely used in power electronic devices and other fields, the defects of which can significantly impact its performance in device fabrication. Laser ultrasonic non-destructive testing (NDT) as a novel and effective approach can detect these defects in real time. This study introduces a numerical model for the SiC NDT that elucidates the dynamic interactions between laser-induced ultrasonic waves and surface defects, and internal defects in SiC, respectively. Results show NDT is an effective way to locate the SiC defect and the ultrasonic waves' vibration amplitude of detection points at defect edges increases by at least 16% compared to adjacent points, with a maximum of 43%. A comparative assessment between surface and internal defect vibration responses for acoustic is also made. For internal defects, the oscillation time of the acoustic wave at the detection point on the surface away from the edge of the defect at the excitation point exceeds that of surface defects by 100 ns, and the amplitude near the excitation point is more pronounced, reaching 1.44 nm, which is 4.2 times that of corresponding surface defects. Additionally, a linear relationship is observed between the arrival time of transmitted Rayleigh Waves (RSR) and internal defect length, with a correlation coefficient of 0.9878. Similarly, a linear relationship is established between the amplitude of reflected Rayleigh Waves (rR) and defect width, with a correlation coefficient of 0.9976, providing an effective way to quantify the inner defect. Furthermore, transient temperature profiles at distinct positions and transient acoustic fields and the relationship of acoustic vibration amplitude increasing with laser spot size under a fixed laser power density are also analyzed. This model provides a theoretical foundation for laser ultrasonic NDT setup and choice of micro-vibration detection device.

Keywords: laser ultrasound; numerical simulation; surface defects; internal defects

check for updates

Academic Editor: Dmitri Donetski

Received: 23 December 2024
Revised: 19 January 2025
Accepted: 21 January 2025
Published: 24 January 2025

Citation: Yin, Y.; Xia, J.; Nie, H.; Yao, B.; Sun, D.; Ma, L.; Li, R.; Li, Z.; Zhang, B. Numerical Simulation Analysis of Laser Ultrasonic Detection of Defects in Silicon Carbide. *Crystals* **2025**, *15*, 125. https://doi.org/10.3390/cryst15020125

Copyright: © 2025 by the authors. Licensee MDPI, Basel, Switzerland. This article is an open access article distributed under the terms and conditions of the Creative Commons Attribution (CC BY) license (https://creativecommons.org/licenses/by/4.0/).

1. Introduction

Silicon carbide (SiC) is a third-generation wide-bandgap semiconductor material with a wide range of potential applications. SiC has a wide band gap of ~3.2 eV, as well as excellent thermal conductivity (3.0–4.9 W/(cm·K)), high breakdown electric field strength (up to 3 MV/cm), high electron saturation drift velocity (2×10^7 cm/s), and the high-power devices prepared by it have many advantages such as high frequency, high voltage, and high-temperature resistance [1–3]. It can be used to create Schottky diodes with low reverse recovery current and fast switching characteristics, field effect transistors (MOSFET) with high input impedance and low on-resistance [4–6], and insulate-gate bipolar transistors (IGBT) for high voltage and high current [7]. Additionally, its high

refractive index and notable second- and third-order nonlinear optical properties, coupled with compatibility with complementary metal oxide semiconductor (CMOS) processes, not only enhance its potential in the power electronics industry but also offer extensive potential applications in the field of photonic integrated circuit [8]. Furthermore, the unique capabilities of SiC in supporting color centers with long spin coherence times and enabling high-Q microresonators and single photon emitters make it a promising material for advancing quantum technologies and photonic devices. The demonstrated generation of Kerr frequency combs at low power levels solidifies its role in enabling next-generation optical frequency comb applications, contributing to both quantum and classical photonic technologies [9,10]. However, during the fabrication and processing of SiC, various defects may arise, which can significantly degrade material performance and reduce the lifetime of devices if not promptly detected and evaluated. Among these, ion implantation-induced defects are also of concern. Considering the critical need for low-loss SiC optical waveguides in integrated photonics, it is imperative to develop advanced non-contact detection and characterization techniques for these defects [11–13]. In particular, we focus on surface defects formed by the epitaxial growth of SiC, such as pits, bumps, and internal thermal cracks caused by excessive laser energy and rapid cooling during laser processing, which propagate along the lattice direction and manifest as elongated cracks. Although these defects may seem insignificant, they all have the potential to be the starting point for the destruction of SiC structures [14,15]. Therefore, in the face of the growing demand for industrial applications of SiC, researchers have been looking for effective detection methods to identify and evaluate defects in SiC production and processing processes online.

Commonly used SiC defect detection methods include non-optical inspection and optical inspection. Non-optical detection methods are relatively well established, including the KOH corrosion method and electron microscopy (EM) [16]. KOH corrosion technology is preferred among them due to its low cost and great efficiency; however, SiC materials will be irreparably damaged by its dissolution process, necessitating additional polishing treatment. The other type of EM inspection can provide nanometer resolution, but the specimen thickness is more demanding, requiring less than 1 μm [17], which makes these two methods not universal and unsuitable for defect detection such as SiC which requires real-time online processing. Optical inspection technology has become an important choice for the requirements of in-line defect inspection, i.e., batch inspection that is non-contact and does not damage the properties of the material. Optical microscopy (OM), optical coherence tomography (OCT), and differential interference contrast (DIC) are three optical inspection techniques that perform well in near-surface defect detection but have certain limitations in deep penetration. To detect subsurface defects, Raman spectroscopy (Raman), X-ray diffraction (XRT), and photoluminescence (PL) have been used, but Raman testing time is long, XRT is expensive, and PL has room for improvement in terms of defect mapping ability and depth resolution [18]. Therefore, with the development of technology, laser ultrasonic testing (LUT) technology has received more attention in non-destructive testing due to its unique advantages, similar to the visualization of the structure by using reflected light in OCT, and the use of laser as the acoustic excitation source and detection source to detect the surface and internal defects of materials, such as cracks, porosity, and inclusions, without contact. It can not only improve the detection efficiency of materials but also avoid the damage caused by traditional contact inspection and provide further support for the analysis of internal defects in materials.

Ultrasonic non-destructive testing technology has developed rapidly in modern times, especially in metal materials such as aluminum and stainless steel. In 1963, White et al. [19] took the lead in proposing the one-dimensional theory of transient heating to produce

elastic waves, that is, when the surface of an object is subjected to instantaneous heating, such as electron bombardment or radio frequency absorption, the surface of the object will produce an uneven displacement due to thermal expansion, and this displacement will also form an elastic wave, which provides an idea for the study of non-destructive detection. In 1968, J. Bushnell [20] carried out theoretical calculations and experimental verification of thermoelastic stress in solids, and the results showed that the shape and absolute amplitude of the stress pulse were in good agreement when the parameters were not adjusted. In 2000, Royer et al. [21] proposed the use of a thermoelastic laser line source to excite ultrasound waves in isotropic solids, and the model determined that the excitation laser can provide a closed form of expression for the surface displacement of surface waves in the near-field and far-field regions when the excitation laser is a Gaussian beam. In 2001, Takao Tanaka and Yasukazu Izawa [22] successfully used a Q-switched Nd: YAG laser to excite ultrasonic waves in a carbon steel sample, and a Fabry–Perot interferometer built by a continuous laser detected internal defects with a diameter of 100 μm, providing a new idea for the industrial detection of structural defects. In 2006, Wang et al. [23] not only evaluated the bond quality between the coating and the aluminum substrate by extracting the amplitude ratio of the ultrasonic reflected wave and the direct wave but also used the amplitude ratio image obtained by the scanning system to reflect the material mass distribution. In 2017, Quintero et al. [24] performed the first laser ultrasonic non-destructive testing of ceramic matrix composites (CMCs), determined the laser power density threshold of the material, and successfully imaged the interlaminar defects of the conforming material. In 2019, Zhang et al. [25] first utilized the 1540 nm pulse lasers to excite surface acoustic waves in pig and living human tissues, and the acoustic wave vibrations were measured by using a 1550 nm Mach–Zehnder Laser Doppler Vibrometer, which demonstrated the imaging capabilities of laser ultrasonics in deep biological tissues. In 2020, Jang et al. [26] developed a high-repetition-rate excitation laser ultrasonic detection system and successfully detected microcracks (less than 10 μm) in silicon wafers by using a high-speed laser Doppler vibrometer to detect acoustic vibrations. This experiment is also the first successful attempt at laser-induced ultrasonic waves of different frequencies to produce nonlinear modulation at cracks and to judge the internal crack parameters of the material by obtaining the signal vibration amplitude. In 2023, Lv et al. [27] conducted circular scans on AlSi10Mg materials using a laser Doppler vibrometer and reconstructed 2D and 3D images of subsurface defects with Gaussian filtering algorithms, thereby validating the effectiveness of laser ultrasonic testing in additive manufacturing components. In 2024, Zheng et al. [28] employed laser ultrasonic technology to assess the microstructure and properties of annealed SLM 316L stainless steel, revealing correlations between ultrasonic characteristics and material microstructure and mechanical properties, offering a new method for rapid non-destructive material property assessment. In conclusion, it is possible to extract material structure parameters by using a pulsed laser to create ultrasonic waves, which can then result in linear or nonlinear changes due to the interaction between sound waves and defects. However, the research on laser ultrasonic non-destructive testing technology for SiC is still in the exploratory stage. Furthermore, for the design of vibration detection equipment in practical industrial applications, it is crucial to ascertain the accuracy requirements and the impact of defect location on the acoustic vibration signal as well as the relationship between defect parameters and the acoustic vibration. Therefore, considering the actual application requirements of SiC industrial online detection, it is necessary to carry out laser ultrasonic simulation of SiC materials.

In the paper, a numerical model is proposed to describe the interaction between the acoustic waves excited by pulsed lasers with different parameters and the defects at various locations in SiC. Compared with other materials, SiC has high hardness, high thermal

conductivity, and good thermoelectric properties [29]. In addition, physical parameters such as the coefficient of thermal expansion, modulus of elasticity, and Poisson's ratio of SiC also have an important impact on the energy absorption efficiency of the laser and the deformation of the material. In this article, the material parameters are set to refer to the typical values for c-axis α-SiC in the COMSOL Multiphysics 6.1 software. Considering the simplification and computational efficiency of the model, the isotropic assumption is preliminarily adopted to define the physical properties of silicon carbide, and Young's modulus and Poisson's ratio based on the average SiC value are set to provide a benchmark model to evaluate the performance of laser ultrasonic technology in the detection process. Thus, the purpose of this paper is to provide a reference for further experiments of laser ultrasonic non-destructive testing of semiconductor materials through simulation.

2. Laser Ultrasound and Numerical Model

The principle of laser ultrasound is to use a pulsed laser to irradiate the surface of the test piece, and a part of the energy is absorbed by the test piece and converted into heat energy. The temperature of the area near the laser irradiation point rises rapidly, thermal expansion is generated currently, and ultrasonic waves are generated under the action of the stress field at this time. Depending on the power density of the pulsed laser, laser ultrasound can be divided into two mechanisms: when the power density of the pulsed laser is lower than the material damage threshold, the process is a thermoelastic mechanism, otherwise it is called an ablation mechanism. Therefore, the thermoelastic mechanism is often used for non-destructive testing of material properties and defects, and the equations involve heat conduction and motion governing equations. For homogeneous isotropic materials, ignoring the effects of thermal convection and radiation on temperature changes, Cartesian coordinates are used in the two-dimensional model, and the heat conduction equation is shown in Equation (1). q is the external heat source of the body heat and can be expressed as Equation (2) [30].

$$\left(\frac{\partial^2 T(x,y,t)}{\partial x^2}+\frac{\partial^2 T(x,y,t)}{\partial y^2}\right)-\frac{\rho c}{K}\frac{\partial T(x,y,t)}{\partial t}=-\frac{q}{K} \tag{1}$$

$$-k\frac{\partial T(x,y,t)}{\partial z}|_{y=h}=q \tag{2}$$

where K is the thermal conductivity, T is the temperature field with time, ρ is the density of the material, c is the specific heat capacity by volume, h is the thickness of the material, and $k=\frac{K}{\rho c}$ is the thermal diffusivity. The acoustic vibration displacement is only related to the material parameters and the temperature field, and its governing equations of motion are shown in Equation (3) [31]. Where λ is the first-order Lame constant of the isotropic solid material, u is the second-order Lame constant, $\boldsymbol{U}$ is the displacement vector, and α is the coefficient of thermal expansion.

$$(\lambda+2u)\nabla(\nabla\cdot U)-u\nabla^2 U-\alpha(3\lambda+2u)\frac{\partial T(x,y,t)}{\partial t}=\rho\frac{\partial^2 \boldsymbol{U}}{\partial t^2} \tag{3}$$

In the numerical model, the absorption of the pulsed laser energy by the specimen occurs on the upper surface, and the heat flux can be expressed as Equation (4) [32].

$$q=AI_0(t)=AI_0 f(x)g(t) \tag{4}$$

where A is the light absorption coefficient, I_0 is the peak power density. $f(x)$ and $g(t)$ represent the spatial and temporal distribution of the laser, respectively, as shown in Equations (5) and (6) [32].

$$f(x) = \exp(-(\frac{(x - x_0)2}{r_0^2})) \tag{5}$$

$$g(t) = \frac{t}{t_0} exp(-\frac{t}{t_0}) \tag{6}$$

The time distribution function $g(t)$ can also be defined as the repetition frequency laser $fre(t)$, as shown in Equation (7).

$$fre(t) = g(mod(t, 1/fre)) \tag{7}$$

Among them, the x_0 is the position of the excitation point, the r_0 is the spot radius, the t_0 is the rise time of the laser, and the fre is the laser repetition frequency.

Equations (8) [33] and (9) [34] describe the approximate center frequency f_{max} and wavelength λ_{min} of the surface wave excited by the pulsed laser under the Gaussian distribution, where the c_R is the surface wave velocity.

$$f_{max} = \frac{\sqrt{2}c_R}{\pi r_0} \tag{8}$$

$$\lambda_{min} = \frac{\pi r_0}{\sqrt{2}} \tag{9}$$

The SiC of the specimen is set as a two-dimensional rectangle of 10 × 5 mm, and the rectangular notch is set as the material defect by differential setting. The laser parameters are defined with a beam radius (r_0) of 100 µm and a rise time of (t_0) 10 ns. The specimen is regarded as a semi-infinite solid, and the irradiation of the pulsed laser belongs to surface heating. To reduce the influence of ultrasonic echoes formed by the action of the left and right boundaries, the remaining boundaries of the specimen are set to be low reflection and adiabatic conditions, as shown in Equations (10) and (11), respectively [35].

$$n \cdot [\sigma - \alpha(3\lambda + 2u)T(x, y, t)I] = 0 \tag{10}$$

$$-k\frac{\partial T}{\partial y}\Big|_{y=0} = -k\frac{\partial T}{\partial x}\Big|_{x=l} = -k\frac{\partial T}{\partial x}\Big|_{x=0} = -AI_0 f(x)g(t) = 0 \tag{11}$$

where n is the normal vector of the surface, σ is the stress tensor, and I is the unit tensor.

Lastly, the initial conditions of the material, along with the time step and spatial resolution for the simulation, are configured. The initial temperature of the specimen is set to 293.15 K, and the initial displacement of the material surface is 0. The meshes of the laser irradiation area and the area near the defect are selected as triangular grids with a minimum of 25 μm, and the rest of the meshes are set to a minimum of 35 μm with a time step of 10 ns.

Typical physical and mechanical parameters of SiC and excitation source parameters in the numerical model are shown in Table 1.

Table 1. Parameters of laser ultrasonic numerical model of silicon carbide and excitation source.

Physical Parameters (Units)	Symbol	Value
density (Kg/m^3)	ρ	2800 [24]
Young's modulus (Pa)	E	5×10^{11}
Poisson's ratio	ν	0.16
Thermal expansion coefficient (1/K)	α	$2.894653 \times 10^{10} - 120032.4 \times T - 69037.36 \times T^2 + 158.6722 \times T^3 - 0.1348974 \times T^4$
Spot radius (mm)	r_0	0.1
Laser rise time (ns)	t_0	10
Peak power density (W/m^2)	I_0	2.5×10^{11}

To explore the difference between the surface defect and the internal defect with the acoustic wave action results, the numerical model first sets up two two-dimensional SiC cross-sections as shown in Figure 1, which contain a surface defect or an internal defect, respectively. The length and height of the specimen are 10 mm × 5 mm, the defect size is 0.1 × 0.05 mm, and (−2,0) is the excitation point position. In the schematic diagram, a scale of 1 mm corresponds to the numerical value 1.

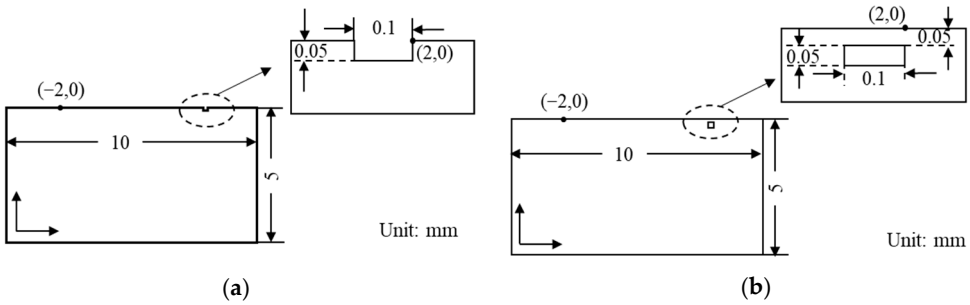

Figure 1. Schematic diagram with a surface defect (**a**) or an internal defect (**b**).

3. Results Analysis

In the numerical simulation, a pulsed laser with a repetition rate of 100 kHz is employed. Figure 2 illustrates the temperature change at the excitation point located at (−2,0) under four pulse excitations. Analysis of this diagram reveals that the temperature at the excitation point increases rapidly due to laser irradiation, followed by a swift decrease once the pulsed laser disappears. Notably, the temperature at the excitation point rises consistently by the same amount after each pulsed laser action, suggesting that the repetition rate can be adjusted to ensure that the maximum surface temperature of the material—specifically, the temperature at the excitation position—remains below the damage threshold. After the fourth pulsed laser action, the maximum surface temperature of the material reaches 720.22 K. Considering that the decomposition temperature of SiC is approximately 1400 °C under atmospheric pressure, which is equivalent to 1673 K, it can be concluded that the thermal elastic mechanism is maintained throughout the four pulses of simulated laser ultrasonic action, thus preventing any thermal damage to the material [36]. Figure 3 presents the temperature change profile at various depths following the first pulse laser action at the excitation point. The temperature distribution is concentrated within the top 10 microns below the material's surface. As the depth from the surface increases, the maximum temperature achievable at the excitation point diminishes significantly, and the decreasing rate slows down. Therefore, the corresponding laser source can be regarded as a surface thermoelastic force source.

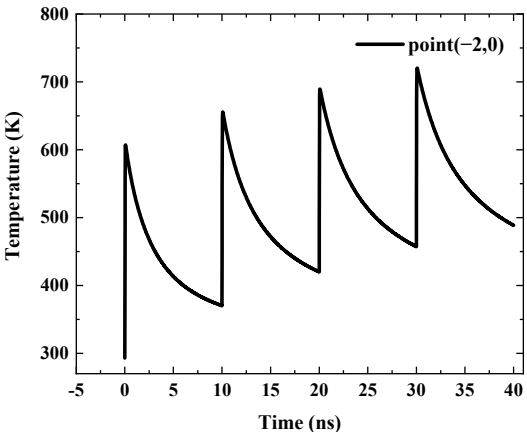

Figure 2. Temperature change curve at the excitation point (−2,0).

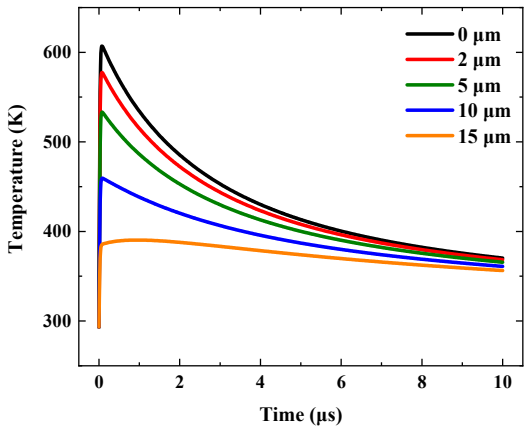

Figure 3. Temporal temperature evolution at various depths following pulsed laser irradiation on SiC.

Figure 4 shows the acoustic field distribution contour of sound waves in SiC materials with a surface defect at different times. As can be seen from the figure, the pressure wave P has the fastest propagation speed, followed by the shear wave S, and finally, the Rayleigh wave R. The direction angle of the pressure wave is greater than that of the shear wave, and the Rayleigh wave propagates along the horizontal surface with a direction angle of 0°. In 2017, R. Quintero also measured that the propagation velocity of pressure waves in ceramic matrix composites is 6850 m/s and that of shear waves is 3280 m/s [24]. According to the acoustic cloud map, the reflection and transmission of each ultrasonic wave after encountering the defect can be observed, and then its mode conversion can be analyzed. For example, as shown in Figure 4a, at t = 350 ns, the P wave is reflected and transmitted after the propagation encounters the defect, which is marked with rP and tP, respectively, in the diagram, and a part of the energy also undergoes a mode transition, becoming a shear wave (PS) and a Rayleigh wave (PR) along the edge and corner of the defect. In terms of energy, the energy of the Rayleigh wave is the strongest and propagates along the surface. After encountering the surface micro-defect, a part of the reflection Rayleigh wave (rR) is formed, as shown in Figure 4b, at the time of t = 700 ns, at this time, due to the small depth of the defect, most of the energy Rayleigh wave continues to propagate along the lower surface of the defect to form a transmitted Rayleigh wave (tR). However, as the depth of the surface defect increases, the energy of the reflected Rayleigh wave will gradually increase. Once the depth of the surface defect increases to more than a certain value, the energy of the reflected echo will be close to stable, because most of the energy of the Rayleigh wave is concentrated in the depth range of half the wavelength of the sound wave from the surface. In addition, a small number of Rayleigh waves are converted into shear waves (RS) and pressure waves (RP) to continue propagating.

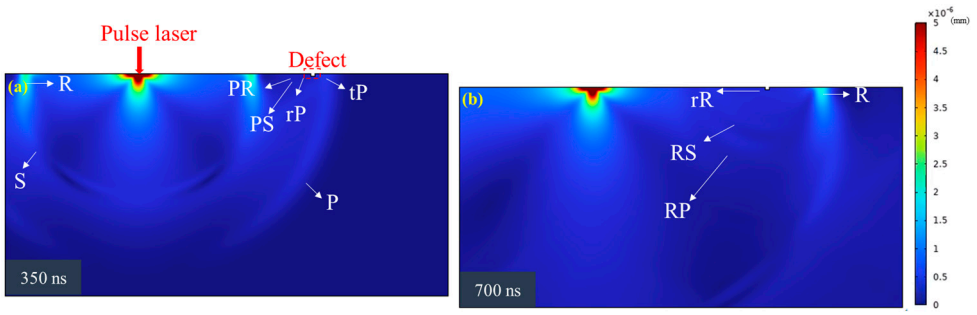

Figure 4. Acoustic field distribution of specimens with a surface defect at (**a**) t = 350 ns and (**b**) t = 700 ns.

As shown in Figure 5, the defect is located 50 μm below the surface of the material, and the propagation path of each sound wave in the material at different times is observed.

Similar to surface defects, as shown in Figure 5a, at t = 550 ns, the Rayleigh wave propagates to the defect location, and most of the energy is transmitted along the upper and lower surfaces of the internal defect to form a transmitted Rayleigh wave (tR), and a small part of the Rayleigh wave interacts with the edge of the internal defect and reflects to generate a reflected Rayleigh wave (rR). Additionally, a mode transition may occur at the upper left and lower left top corners of the defect, leading to the generation of a converted Rayleigh wave (RSR) [35], and the right edge will interact with the Rayleigh wave to generate an oscillating wave. As shown in Figure 5b, at t = 700 ns, the Rayleigh wave and the defect have a more obvious mode transition than the surface defect, and the Rayleigh wave converts the shear wave (RS) and the Rayleigh wave transforms the pressure wave (RP). Notably, as the depth of the internal defect increases to surpass the wavelength of the Rayleigh wave, the energy of the rR diminishes nearly to zero, while the corresponding transmitted Rayleigh wave passes through entirely. At this juncture, the influence of the internal defect depth on the vibrational displacement is solely mediated by pressure wave (P) and shear wave (S).

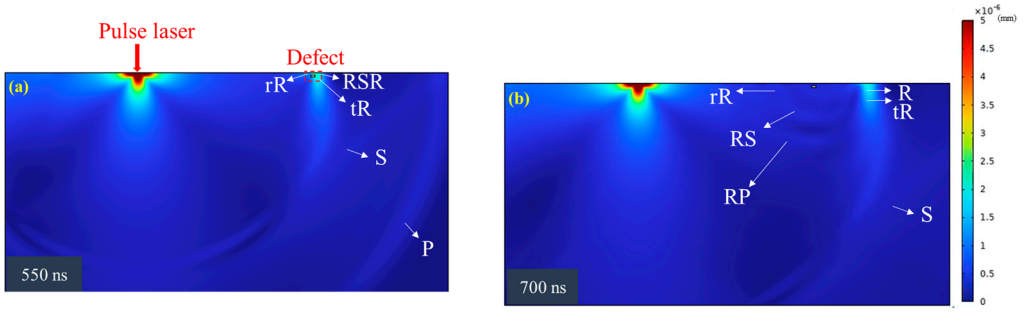

Figure 5. Shows the distribution of the sound field at (**a**) t = 550 ns and (**b**) t = 700 ns of a specimen with an internal defect.

Unlike surface defects, the upper and lower surfaces of the internal defect will interact with sound waves. Specifically, at the vertical surface detection point corresponding to the edge of the internal defect, namely (1.9,0), the direct surface wave and the reflected wave from different times can be received. Within this portion of the reflected wave, signals resulting from the interaction of the acoustic wave with the corner of the left edge of the defect (RSR) and the upper surface of the defect (rR) are encapsulated. On the contrary, for the edge point of the surface defect, the reflected Rayleigh wave (rR) is generated when the direct wave reaches the left edge of the defect, so the reflected Rayleigh wave will "disappear" at the edge detection point of the surface defect, and the amplitude of the direct Rayleigh wave will increase sharply. This not only provides an idea for the subsequent observation of the edge position of the defect but also lays the foundation for judging the surface defect and the internal defect.

Figure 6 shows the reflected and transmitted waves of the defective specimen in the time domain, respectively, with Figure 6a showing the vibration image at (1,0) and Figure 6b showing the vibration image at (4,0). Firstly, it is observed that the ultrasonic waveform of isotropic SiC material exhibits a pattern similar to that observed in aluminum material since they have similar ultrasonic parameters [35]. Consequently, this material can be utilized as an ideal early-stage model for investigating the differential effects of surface and internal defects on ultrasonic wave propagation in SiC [24]. Moreover, the calculated propagation velocities are approximately 13 km/s for the pressure wave, 8333 m/s for the shear wave, and 7317 m/s for the surface wave, which differ notably from those measured in ceramic matrix composites. Nevertheless, the core objective of this study is to analyze the impacts of internal and surface defects on the waveforms and amplitudes using laser

ultrasonic techniques. This focus remains pertinent irrespective of the material's isotropic or anisotropic nature.

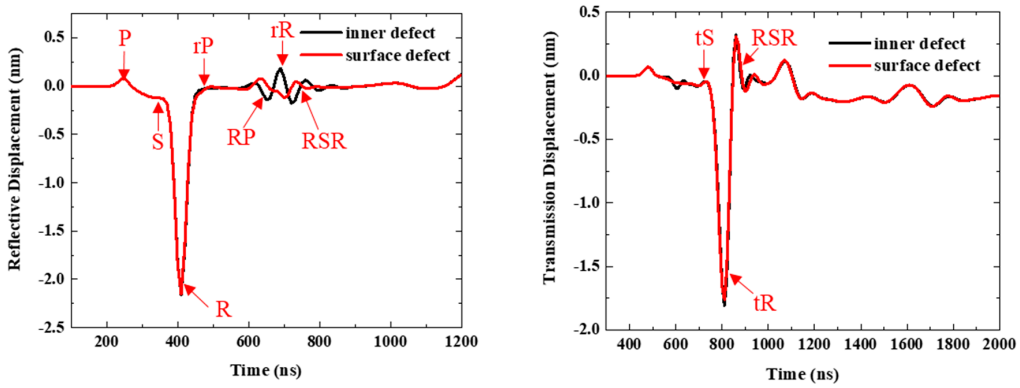

(**a**) (**b**)

Figure 6. Time domain diagram of the reflected wave signal measured at (1,0) (**a**) and the transmitted wave signal measured at (4,0) (**b**).

The perpendicular surface detection points corresponding to the defect edge are (1.9,0) and (2,0), respectively. The surface detection point signals of the specimen with a surface defect or an internal defect are compared, as shown in Figure 7, including the reflected wave signal between (0,0) and (1.9,0), and the transmitted wave signal on the right side of (2,0). From Figure 7a, it is evident that as the detection point recedes from the excitation source, the direct wave signal progressively displaces to the right, and the vibration amplitude diminishes in tandem with the attenuation of the acoustic wave energy. Notably, the vibration amplitude at detection points (1.9,0) and (2,0), situated adjacent to the defect edge, surges dramatically, attaining the maximum amplitude. For surface defect, the amplitudes recorded at (1.9,0) and (2,0) reach 2.85 nm and 2.87 nm respectively, representing an increase of 0.62 nm and 0.55 nm over adjacent points. In the context of internal defects, as shown in Figure 7b, the amplitudes at these same points escalate to 3.39 nm and 2.61 nm, respectively, a rise of 1.02 nm and 0.36 nm compared to neighboring points. Additionally, amplitudes at edge detection points consistently surpass those of adjacent points by an average of 16%, with a maximum discrepancy of up to 43%. This phenomenon is attributable to the energy dissipation experienced during the propagation of the acoustic wave. Moreover, the Rayleigh wave at the edge of the defect exhibits a predisposition to mode conversion, especially the RSR wave. However, the direct Rayleigh wave at the defect edge overlaps with a segment of the reflected wave or the transmitted wave, leading to an escalation in the amplitude at the defect edge detection point and a concomitant alteration in the waveform.

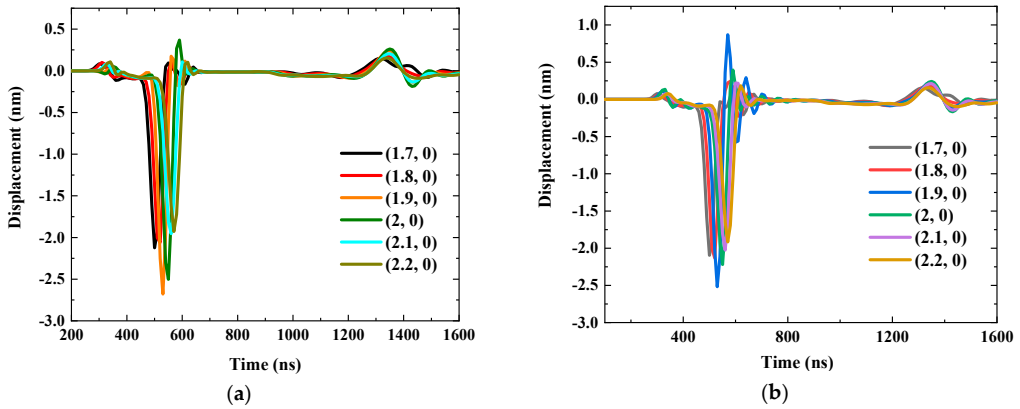

(**a**) (**b**)

Figure 7. Surface inspection points of SiC specimens with a surface defect (**a**) or with an internal defect (**b**).

For the internal defect, as illustrated in Figure 7b, the observed phenomenon mirrors that of surface defect. Furthermore, the vibration amplitude of the signal encompassing the internal defect markedly surpasses that of the vibration signal containing the surface defect at the surface detection point corresponding to the edge of the near excitation point of the defect, which is 19% greater than that of the surface defect. This discrepancy arises because, in the specimen harboring internal defects, the Rayleigh wave signal concentrated near the surface traverses along the upper surface of the defect. Conversely, in the specimen containing surface defects, the majority of the ultrasonic signal undergoes multiple reflections and scatterings at the defect edge, leading to the dissipation of the energy of the ultrasonic signal propagating along the surface.

To facilitate a more apparent comparison of vibration signals between the surface and internal defect, the waveform signals of perpendicular surface detection points corresponding to the defect edges are selected, as depicted in Figure 8. Figure 8a presents the waveform at the (1.9,0) detection point, which is at the edge of the defect on the same side of the excitation point, while Figure 8b displays the waveform at the (2,0) detection point, which is at the edge of the defect on the opposite side of the excitation point.

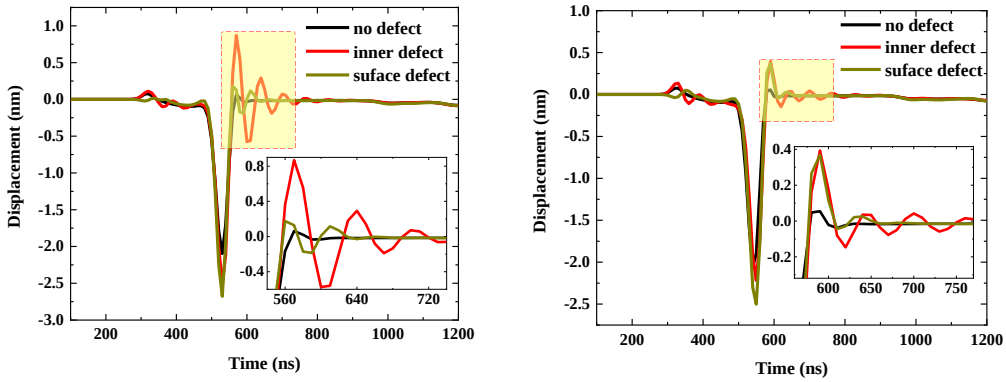

Figure 8. Detection points at the edge of the defect on the same side of the excitation point (**a**) and on the opposite side of the excitation point (**b**).

It can be observed that the material with an internal defect exhibits significant vibration signals at the defect edges. Near the excitation point, the vibration signal amplitude of the oscillation signal reaches 1.44 nm, while surface defects show weaker vibration signals with an amplitude of approximately 0.34 nm. At defect edges further from the excitation point, the vibration signal amplitude in defect-free conditions is significantly lower than that of both with a surface or an internal defect, the one with the internal defect exhibiting more pronounced oscillation signals, which lasts for 270 ns, exceeding that of a surface defect by over 100 ns. This observed phenomenon is attributed to the fact that the reflected and transmitted waves of internal defect are not solely influenced by the Rayleigh wave with the edge near the side of the defect but also by the interaction of the upper and lower surfaces of the internal defect and the apex angle of the internal defect with the Rayleigh wave. In summary, the method for determining defect location involves first identifying the edge of the defect and subsequently discerning between surface and internal defects by assessing the presence or absence of an obvious oscillating signal. This approach offers valuable insights for online non-destructive testing in distinguishing defect locations.

To study the influence of SiC thermal crack, i.e., internal defect parameters, on Rayleigh wave, the influence of crack length on transmitted wave signal is first tested. As shown in schematic Figure 9, the RSR wave is generated at the lower left corner of the internal defect. A portion of the wave reflects along the left edge, while another part transmits along the bottom and right edges of the defect, eventually reaching the (3,0) detection point. After

the defect location is determined, the depth of the internal defect from the surface and the crack width is fixed at 0.05 mm, the left edge of the defect from the excitation point remains unchanged, the defect length continues to expand to the right, and the defect length varies from 0.1 mm to 0.7 mm in 0.1 mm steps.

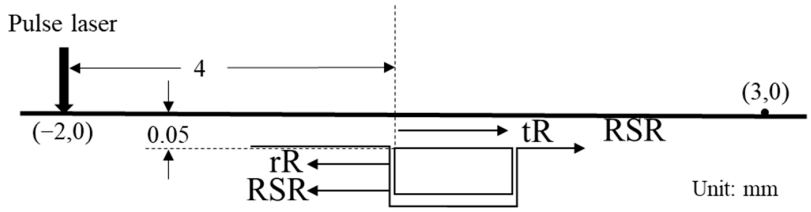

Figure 9. Schematic diagram of the estimated length and width of the internal defect.

As illustrated in Figure 10, at the detection point (3,0), the arrival time of the transmitted wave (tR) remains consistent, while the arrival time of the Rayleigh wave (RSR) experiences a delay. In 2019, C. Tao [37] quantitatively characterized the influence of aluminum surface defect parameters on the arrival time of Rayleigh waves, estimating the length and width parameters of surface defects by utilizing the characteristics of Rayleigh wave propagation near the surface, specifically along the edge of the defect and the material surface. Additionally, it was discovered that the RSR wave is generated at the lower left vertex where the Rayleigh wave intersects with the internal defect, subsequently propagating along the lower surface and right edge of the internal defect to the detection point. As depicted in Figure 11, the correspondence between the arrival time of the RSR wave and the length of the defect is plotted, and a linear relationship can be expressed as $y = 450x + 670$, with a determination coefficient $R^2 = 0.9878$. This indicates that the velocity of the sound changes little during the propagation, and it is a feasible method to calculate the length of the internal defect by using the arrival time of the RSR wave located at a point on the opposite side relative to the excitation point and the defect.

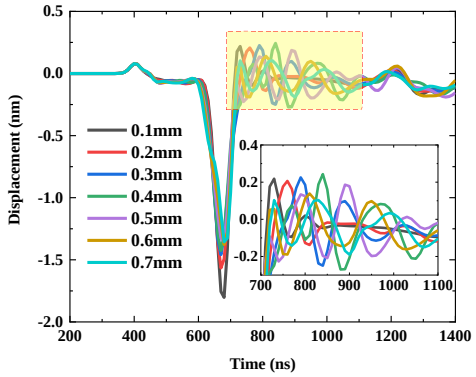

Figure 10. Transmitted wave vibration image with different internal defect lengths.

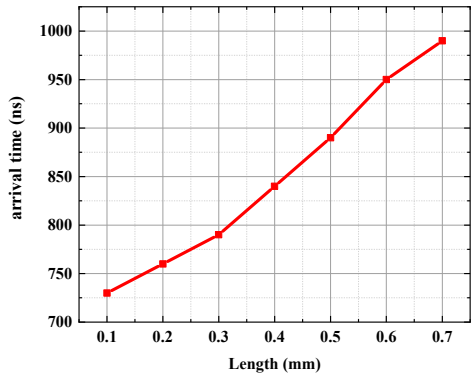

Figure 11. Defect length and RSR wave arrival time relationship.

Next, the internal defect length and depth are fixed at 0.1 mm and 0.05 mm, respectively, and the defect width varies from 0.01 mm to 0.07 mm in 0.01 mm steps. Figure 12 shows the vibration diagram of the reflected wave detected at (1,0) for defects of different widths, in which it can be clearly observed that the arrival time and amplitude of the direct wave are the same for different defects. The amplitude of the reflected Rayleigh wave rR increases with the increase of the width of the internal defect, but the arrival time has almost no effect. This phenomenon occurs because the Rayleigh wave can reach a distance of approximately one wavelength below the surface of the specimen. According to Equation (9), one wavelength is calculated to be approximately 222 μm. Before reaching a depth of one wavelength, the energy of the reflected Rayleigh wave increases as the width of the internal defect increases. As depicted in Figure 13, when the internal defect varies in width from 0.01 mm to 0.07 mm at a depth of 0.01 mm, the corresponding relationship between the amplitude of the reflected Rayleigh wave and the defect width is plotted. The linear relationship is expressed as y = 6.7954x + 0.0115, with a determination coefficient of 0.9976, indicating a robust linear relationship.

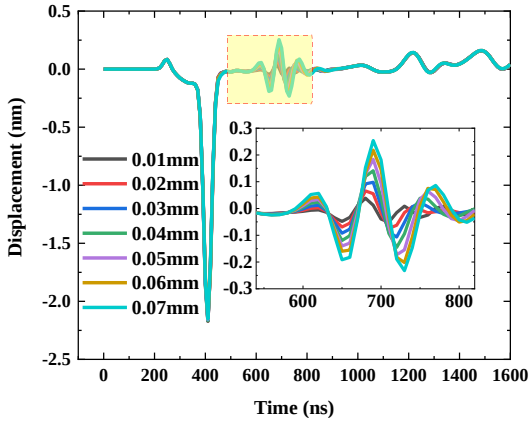

Figure 12. Reflected wave vibration images with different defect widths.

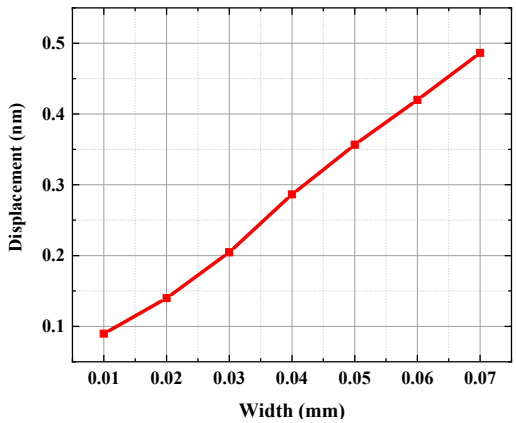

Figure 13. Relationship between defect width and rR wave amplitude.

The magnitude of the laser energy is directly proportional to the magnitude of the stress wave, and when the power density is fixed, changing the spot radius will not only affect the energy of the single pulse but also affect the stress field distribution. By fixing the laser power density of 2.5×10^{11} W/m^2, the length and depth of the internal defects are 0.1 mm and 0.05 mm, respectively. The spot radius changes from 25 μm to 200 μm, and the waveforms of the ultrasonic wave are observed. The vibration waveform is shown in Figure 14. As the radius of the spot increases from 25 μm, the more the heat absorbed by the

material, the greater the amplitude of the sound wave vibration, especially the amplitude of the Rayleigh wave, but the amplitude is not nonlinear with the increase of the radius.

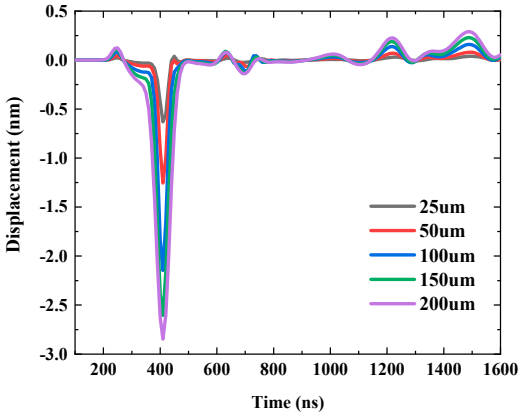

Figure 14. Acoustic wave vibration images with different spot radii.

As the spot radius increases, the growth rate of the sound wave vibration amplitude gradually slows down. In practical applications, to ensure that the signal vibration is sufficiently evident, the signal amplitude is often increased by enhancing the laser power density, thereby ultimately improving the signal-to-noise ratio. However, this procedure also causes damage to the material's surface, making it crucial to select an appropriate spot radius and power density to optimize the signal-to-noise ratio. Through this simulation experiment, it is discovered that the spot radius can be appropriately increased when the laser power density is fixed to obtain the required large signal. Moreover, during non-destructive measurement of surface defect parameters, the defect parameters can also be determined by varying the spot radius. Specifically, when the spot radius equals the length of the surface defect, the distribution range of the thermal effect is established, and the sound wave will scatter upon encountering the defect, potentially interfering with the scattered wave within the defect area, thus enhancing the ultrasonic amplitude to a certain extent.

Based on the aforementioned analysis, it is evident that when the energy of a single pulse is configured to approximately 60 μJ within this numerical model, the vibration amplitude of the sound wave predominantly ranges from 1 nm to 3 nm. Referring to the Technical Specification for Environmental Vibration Monitoring (HJ 918-2017), commercial vibration sensors should possess the capability to measure vibrations extending up to several megahertz, and even vibrations at GHz frequencies. Additionally, the accuracy standards for ultrasonic testing equipment dictate a lower limit of not less than 50 dB, implying that the minimum detectable acoustic vibration amplitude within the numerical model should not fall below 30 fm, and the resolution could be detected by the reported apparatus Polytec MSA-600. Consequently, in practical scenarios involving small displacement detection, taking into account the light absorption capacity of the material across various environments, enhancing the signal-to-noise ratio can be achieved by either increasing the single pulse energy or determining an optimal spot radius to elevate the vibration amplitude while ensuring it remains below the damage threshold.

4. Summary

This study employs a numerical model simulation to investigate laser-excited ultrasonic waves in isotropic silicon carbide (SiC) materials and their interactions with surface and internal defects. Similar to extant laser ultrasound simulation models, this study also adopts the finite element method for the simulation. However, prior studies by C. Chen [35], C. Tao [37], and Y. Liu [38], which explored the interactions of Rayleigh waves

with surface defects and their relationship to defect dimensions, did not address several key gaps in understanding. Specifically, these gaps include (1) the distinct acoustic responses of surface versus internal defects and (2) the quantification of internal defect dimensions. This research addresses these limitations by focusing on silicon carbide, offering a novel approach to distinguish between surface and internal defects through the oscillation time and the amplitude of vibration., along with quantifying the dimensions of internal defects. Notably, it establishes robust linear relationships for the length and width of internal defects, achieving coefficients of determination (R^2) of 0.9878 and 0.9976, respectively. Furthermore, it investigates the impact of spot size on amplitude, providing insights to optimize laser ultra-sound inspection parameters and enhance detection accuracy and sensitivity.

The simulation analyzes the temperature field distribution around the excitation point under repetitive laser excitation and the transient acoustic field contours at various times. Under a pulsed laser operating at 100 kHz repetition rate and 2.5×10^{11} W/m^2 power density, periodic fluctuations in surface temperature are induced at the excitation point without ablation of the SiC material's surface, with the peak temperature at 607 K, 654 K, 689 K, and 720 K, respectively. At various depths, the temperature at each point decays exponentially with time, and below 15 μm, the temperature profiles stabilize with no significant further changes. Furthermore, the simulation results indicate that the identification of defect edges can be determined by the abrupt increase in the amplitude of Rayleigh waves. This observation holds true for both surface and internal defects, where the amplitude at the vertical surface detection point corresponding to the defect edge is at least 16% higher than that of adjacent detection points, with the maximum increase reaching 43%. Additionally, reflection waves from internal defects exhibit distinct oscillatory behavior due to interactions at defect edges and apexes, particularly in the case of RSR waves. Specifically, compared to surface defects, the ultrasonic oscillation signal amplitudes at defect edges on the same side as the excitation source are significantly higher, reaching 1.44 nm, which is 4.2 times greater than the 0.34 nm observed for surface defect, and the duration of oscillation waves at detection points on the opposite side exceeds that of a surface defect by over 100 ns, with an internal defect exhibiting a duration of 270 ns, offering a robust method for differentiating between internal and surface defects after localization. By the simulation calculation, results indicate that the presence of internal defects can be inferred by observing the sudden amplitude increase near the defect edge, followed by the analysis of the amplitude and duration of the oscillation signal.

The study also examines the linear relationship between sound wave arrival time and amplitude at different detection positions, with determination coefficients exceeding 0.98, indicating a high degree of correlation. The linear correlation between the arrival time of the transmitted Rayleigh surface wave (RSR) and the length of the internal defect, along with the linear relationship between the reflected Rayleigh (rR) and the width of the internal defect, allows for approximating the defect size. Additionally, the effect of internal defect parameters and pulsed laser spot radius on acoustic vibrations is also explored. Maintaining a constant laser power density while progressively expanding the spot radius from 25 μm, 50 μm to 100 μm, results in a nearly linear amplification of the amplitude of acoustic wave vibrations. This study not only lays a theoretical groundwork for the quantitative detection of surface and internal defects in semiconductor materials like SiC but also implies that adjusting the spot radius can modulate vibration amplitude in future commercial vibration detection applications, thereby substantially enhancing the signal-to-noise ratio of vibration detection devices.

Regarding the limitations, our methodology quantifies internal defect widths utilizing the energy of reflected Rayleigh waves, demonstrating an approximately linear correlation for defect widths below 0.15 mm. The practical threshold is governed by the combined

measure of the defect width and its proximity to the surface, which should not surpass the minimum wavelength of the Rayleigh waves. Concerning defect length evaluation, a minimal length of 0.05 mm is essential to establish a discernible linear relationship through transmitted Rayleigh waves.

In future research endeavors, we will comprehensively investigate the influence of the anisotropy of SiC materials on ultrasonic propagation characteristics as well as the goal of quantifying a broader spectrum of defect shapes. This exploration will encompass, but not be limited to, examining the effects of various crystal orientations and grain boundaries on ultrasonic propagation velocity and attenuation, delving into the impact of anisotropy on the sensitivity and accuracy of defect detection, and utilizing machine learning to process various defect shapes. Mach–Zehnder and Sagnac interferometry techniques will be used in Laser Doppler vibrometry (LDV) investigations [39,40]. These have been employed in micro-vibration to analyze the modalities of outdoor tilting rotating blades and track the vibration characteristics of mobile railway carriages [41,42]. Our research will concentrate on algorithmic advancements and system optimization for precise vibration displacement and velocity measurement. To improve the performance of the LDV system for SiC materials, novel scanning methods such as conical and circular scanning will be tested. The accuracy of online non-destructive testing in real-world laser processing and other industrial applications will be improved by these investigations, which will also greatly improve our understanding of laser ultrasonic non-destructive testing of semiconductor materials.

Author Contributions: Conceptualization, Y.Y.; software, Y.Y.; investigation, D.S. and L.M. and R.L. and Z.L.; resources, H.N. and B.Y. and B.Z.; writing—original draft preparation, Y.Y.; writing—review and editing, J.X. All authors have read and agreed to the published version of the manuscript.

Funding: This research was funded by the Key Research and Development Program of Shandong Province (No.2020CXGC010104, No.2022JMRH0102), National Natural Science Foundation of China (62475135, 62322509) and Shandong Provincial Natural Science Foundation (ZR2024MF074).

Data Availability Statement: The data in this study are available upon request.

Conflicts of Interest: The authors declare no conflicts of interest.

References

1. Mehregany, M.; Zorman, C.A. SiC MEMS: Opportunities and challenges for applications in harsh environments. *Thin Solid Film.* **1999**, *355–356*, 518–524. [CrossRef]
2. Papanasam, E.; Kumar, B.P.; Chanthini, B.; Manikandan, E.; Agarwal, L. A Comprehensive Review of Recent Progress, Prospect and Challenges of Silicon Carbide and its Applications. *Silicon* **2022**, *14*, 12887–12900. [CrossRef]
3. Tsunenobu, K. Material science and device physics in SiC technology for high-voltage power devices. *Jpn. J. Appl. Phys.* **2015**, *54*, 040103. [CrossRef]
4. Sugawara, Y.; Takayama, D.; Asano, K.; Singh, R.; Palmour, J.; Hayashi, T. 12-19 kV 4H-SiC pin diodes with low power loss. In Proceedings of the 13th International Symposium on Power Semiconductor Devices & ICs. IPSD '01, Osaka, Japan, 7 June 2001; IEEE: New York, NY, USA, 2001. [CrossRef]
5. Abbatelli, L.; Catalisano, G.; Stella, C.G. SiC and Silicon MOSFET solution for high frequency DC-AC converters. In Proceedings of the PCIM Europe 2018: International Exhibition and Conference for Power Electronics, Intelligent Motion, Renewable Energy and Energy Management, Nuremberg, Germany, 5–7 June 2018.
6. Brown, J.; Moxey, G. Power MOSFET Basics: Understanding MOSFET Characteristics Associated with the Figure of Merit. 2003; Available online: https://www.vishay.com/docs/71933/71933.pdf (accessed on 23 December 2024).
7. Wang, J.; Huang, A.Q.; Sung, W.; Liu, Y.; Baliga, B.J. Smart grid technologies. *IEEE Ind. Electron. Mag.* **2009**, *3*, 16–23. [CrossRef]
8. Ou, H.; Shi, X.; Lu, Y.; Kollmuss, M.; Steiner, J.; Tabouret, V.; Syväjärvi, M.; Wellmann, P.; Chaussende, D. Novel Photonic Applications of Silicon Carbide. *Materials* **2023**, *16*, 1014. [CrossRef]
9. Wang, C.; Fang, Z.; Yi, A.; Yang, B.; Wang, Z.; Zhou, L.; Shen, C.; Zhu, Y.; Zhou, Y.; Bao, R.; et al. High-Q Microresonators on 4H-Silicon-Carbide-on-Insulator Platform for Nonlinear Photonics. *Light Sci. Appl.* **2021**, *10*, 139. [CrossRef] [PubMed]

10. Castelletto, S.; Peruzzo, A.; Bonato, C.; Johnson, B.C.; Radulaski, M.; Ou, H.; Kaiser, F.; Wrachtrup, J. Silicon Carbide Photonics: Bridging Quantum Technology. *ACS Photonics* **2022**, *9*, 1434–1457. [CrossRef]
11. Waltl, M. Defect Spectroscopy in SiC Devices. In Proceedings of the 2020 IEEE International Reliability Physics Symposium (IRPS), Dallas, TX, USA, 28 April 2020–30 May 2020; IEEE: New York, NY, USA, 2020. [CrossRef]
12. St, G.M.; Glass, R.C.; Hobgood, H.M.; Tsvetkov, V.F.; Brady, M.; Henshall, D.; Malta, D.; Singh, R.; Palmour, J.; Carter, C.H., Jr. Progress in the industrial production of SiC substrates for semiconductor devices. *Mater. Sci. Eng. B* **2001**, *80*, 327–331. [CrossRef]
13. Shi, X.; Lu, Y.; Chaussende, D.; Rottwitt, K.; Ou, H. Wet-Oxidation-Assisted Chemical Mechanical Polishing and High-Temperature Thermal Annealing for Low-Loss 4H-SiC Integrated Photonic Devices. *Materials* **2023**, *16*, 2324. [CrossRef] [PubMed]
14. Chen, J.P.; Gu, L.; He, G.J. A review on conventional and nonconventional machining of SiC particle-reinforced aluminum matrix composites. *Adv. Manuf.* **2020**, *8*, 279–315. [CrossRef]
15. Sun, D.-R.; Wang, G.; Li, Y.; Yu, Y.; Shen, C.; Wang, Y.; Lu, Z. Laser drilling in silicon carbide and silicon carbide matrix composites. *Opt. Laser Technol.* **2024**, *170*, 110166. [CrossRef]
16. Chen, P.-C.; Miao, W.-C.; Ahmed, T.; Pan, Y.-Y.; Lin, C.-L.; Chen, S.-C.; Kuo, H.-C.; Tsui, B.-Y.; Lien, D.-H. Defect Inspection Techniques in SiC. *Nanoscale Res. Lett.* **2022**, *17*, 30. [CrossRef] [PubMed]
17. Hristu, R.; Stanciu, S.G.; Tranca, D.E.; Matei, A.; Stanciu, G.A. *Nonlinear Optical Imaging of Defects in Cubic Silicon Carbide Epilayers*; Nature Publishing Group: London, UK, 2015. [CrossRef]
18. Berwian, P.; Kaminzky, D.; Rosshirt, K.; Kallinger, B.; Friedrich, J.; Oppel, S.; Schneider, A.; Schütz, M. Imaging Defect Luminescence of 4H-SiC by Ultraviolet-Photoluminescence. *Diffus. Defect Data Solid State Data Part B Solid State Phenom.* **2016**, *242*, 484–489. [CrossRef]
19. White, R.M. Elastic Wave Generation by Electron Bombardment or Electromagnetic Wave Absorption. *J. Appl. Phys.* **1963**, *34*, 2123–2124. [CrossRef]
20. Bushnell, J.C. Thermoelastic Stress Production in Solids. *J. Appl. Phys.* **1968**, *39*, 5541–5546. [CrossRef]
21. Royer, D.; Chenu, C. Experimental and theoretical waveforms of Rayleigh waves generated by a thermoelastic laser line source. *Ultrasonics* **2000**, *38*, 891–895. [CrossRef] [PubMed]
22. Tanaka, T.; Izawa, Y. Nondestructive Detection of Small Internal Defects in Carbon Steel by Laser Ultrasonics. *Jpn. J. Appl. Phys.* **2001**, *40*, 1477–1481. [CrossRef]
23. Wang, H.; Qian, M.L.; Liu, W. Laser ultrasonic characterization of adhesive bonds between epoxy coating and aluminum substrate. *Ultrasonics* **2006**, *44*, e1349–e1353. [CrossRef] [PubMed]
24. Quintero, R.; Simonetti, F.; Howard, P.; Friedl, J.; Sellinger, A. Noncontact laser ultrasonic inspection of Ceramic Matrix Composites (CMCs). *NDT E Int.* **2017**, *88*, 8–16. [CrossRef]
25. Zhang, X.; Fincke, J.R.; Wynn, C.M.; Johnson, M.R.; Haupt, R.W.; Anthony, B.W. Full noncontact laser ultrasound: First human data. *Light Sci. Appl.* **2019**, *8*, 11. [CrossRef] [PubMed]
26. Jang, J.; Liu, P.; Kim, B.; Kim, S.-W.; Sohn, H. Silicon wafer crack detection using nonlinear ultrasonic modulation induced by high repetition rate pulse laser. *Opt. Lasers Eng.* **2020**, *129*, 106074. [CrossRef]
27. Lv, G.; Yao, Z.; Chen, D.; Li, Y.; Cao, H.; Yin, A.; Liu, Y.; Guo, S. Fast and high-resolution laser-ultrasonic imaging for visualizing subsurface defects in additive manufacturing components. *Mater. Des.* **2023**, *225*, 111454. [CrossRef]
28. Zheng, L.; Yin, A.; Xu, D.; Lu, Y.; Liao, W.; Chen, H.; He, Y.; Xia, Z.; Ma, K.; Yan, X. Nondestructive evaluation of microstructure and mechanical property of post-processing annealed selective laser melted 316L stainless steel by laser ultrasonics. *Phys. Scr.* **2024**, *99*, 105031. [CrossRef]
29. Xu, M.; Girish, Y.R.; Rakesh, K.P.; Wu, P.; Manukumar, H.M.; Byrappa, S.M.; Udayabhanu; Byrappa, K. Recent advances and Challenges in Silicon Carbide (SiC) Ceramic Nanoarchitectures and their Applications. *Mater. Today Commun.* **2021**, *28*, 102533. [CrossRef]
30. Ruipeng, G.; Haitao, W.; Jianyan, Z. Non-contact detection of low carbon steel using laser generated ultrasound at high temperature. *Opt.—Int. J. Light Electron Opt.* **2017**, *136*, 536–542. [CrossRef]
31. Zhang, K.; Zhou, Z.; Zhou, J.; Sun, G. Characteristics of laser ultrasound interaction with multi-layered dissimilar metals adhesive interface by numerical simulation. *Appl. Surf. Sci.* **2015**, *353*, 284–290. [CrossRef]
32. Cao, D.; Wang, K.; Yang, Y. Finite elements simulation of temperature field of thin tubes irradiated by ring lasers. *Laser Technol.* **2010**, *34*, 753–756.
33. Luo, Y. Study on Finite Element Analysis and Signal Testing Methods of Laser-Generated Ultraosonic. Doctoral Thesis, National University of Defense Technology, Changsha, China, 2012.
34. Zhang, Y. Study of Detecting Metal Surface Defects Based on Laser Ultrasound Technology. Doctoral Thesis, Dalian University of Technology, Dalian, China, 2015.
35. Chen, C.; Ju, B.-F.; Yang, X.; Wang, C.; Sun, A.; Gong, J.; Li, Z. All-optical laser-ultrasonic technology for width and depth gauging of rectangular surface-breaking defects. *Rev. Sci. Instrum.* **2021**, *92*, 054901. [CrossRef] [PubMed]

36. DiCarlo, J.A.; Yun, H.-M.; Morscher, G.N.; Bhatt, R.T. *SiC/SiC Composites for 1200 °C and Above*; Springer: New York, NY, USA, 2024. [CrossRef]
37. Tao, C.; Yin, A.; Ying, Z.; Wang, Y.; Shu, X. Numerical study on the mechanism of laser-generated Rayleigh waves' interaction with a surface notch at high temperature. *Jpn. J. Appl. Phys.* **2019**, *58*, 046504.1–046504.9. [CrossRef]
38. Liu, Y.; Peng, Z.; Liu, S.; Hu, P. Numerical simulation of laser ultrasonic detection of the surface microdefects on laser powder bed fusion additive manufactured 316L stainless steel. *Theor. Appl. Mech. Lett.* **2022**, *12*, 100398. [CrossRef]
39. Carolan, T.A.; Reuben, R.L.; Barton, J.S.; Jones, J.D.C. Fiber optic Sagnac interferometer for on-line acoustic emission monitoring of high-temperature power plant structures. *Proc Spie* **1996**, *2868*, 530–539. [CrossRef]
40. Hecht, E. *Optics*; Addison Wesley: Reading, MA, USA, 1987; Section 9-4.
41. Kaynardag, K.; Yang, C.; Salamone, S. An impulsive noise filter for rail vibration measurements using a laser Doppler vibrometer on a moving platform. *Mech. Syst. Signal Process.* **2025**, *223*, 111918. [CrossRef]
42. Hu, Y.; Zhu, W.; Yu, K.; Yang, Y.; Kang, Y. Operational modal analysis of outdoor slanted rotational blades under natural excitation using a long-range tracking continuously scanning laser Doppler vibrometer. *Opt. Laser Technol.* **2025**, *181*, 111516. [CrossRef]

Disclaimer/Publisher's Note: The statements, opinions and data contained in all publications are solely those of the individual author(s) and contributor(s) and not of MDPI and/or the editor(s). MDPI and/or the editor(s) disclaim responsibility for any injury to people or property resulting from any ideas, methods, instructions or products referred to in the content.